Available online at www.sciencedirect.com
ScienceDirect
Trans. Nonferrous Met. Soc. China 34(2024) 1365−1379
Transactions of Nonferrous Metals Society of China
www.tnmsc.cn

Generalized stability criterion for columnar to equiaxed grain transition during solidification upon vertical twin roll casting

Pan WU[1*], Jia-qi HU[1*], Yu-bing ZHANG[1], Shao-jie SONG[1], Yong LI[2], Hui-yuan WANG[3], Guo YUAN[2], Feng LIU[1,4]

1. State Key Laboratory of Solidification Processing, Northwestern Polytechnical University, Xi'an 710072, China;
2. State Key Laboratory of Rolling and Automation, Northeastern University, Shenyang 110819, China;
3. State Key Laboratory of Super Hard Materials, Jilin University, Changchun 130012, China;
4. Analytical & Testing Center, Northwestern Polytechnical University, Xi'an 710072, China

Received 9 November 2022; accepted 11 May 2023

Abstract: To promote the columnar to equiaxed grain transition (CET) to obtain uniform equiaxed grain, most of the available theoretical works mainly focus on the growth but ignore the nucleation. Regarding it, a systematical framework integrating nucleation catalyzed by refiners with dendritic growth, was constructed, where, a new conception of generalized stability (GS), considering evolving thermodynamic driving force (ΔG) and kinetic energy barrier (Q) upon solidification of VTC, was adopted to study the CET position, the grain radius and the mechanical properties. By adding the refiners, especially the Al−5Ti−1B refiner, the larger thickness of 5−6 mm for equiaxed grain and finer grain radius of 19 μm are exhibited by increasing the ΔG for nucleation and the GS for growth, possessing simultaneously improved strength and plasticity. Following a criterion of high ΔG−high GS, the refiner diameter is optimized to be 0.3 μm.

Key words: generalized stability; refiner; columnar to equiaxed grain transition; twin roll casting

1 Introduction

Upon solidification, a transition from columnar to equiaxed growth commonly takes place when nucleation of equiaxed grains occurs in the liquid ahead of the columnar zone, i.e., so-called columnar to equiaxed grain transition (CET) [1,2]. A better understanding or control of the CET (i.e., either eliminating or enhancing it) is of great technical and economic importance, particularly in vertical twin roll casting (VTC) involving a typical sub-rapid solidification. In the VTC of alloys, the columnar dendrite grows easily near the edge of sheets due to positive temperature gradient (TG), whereas, the equiaxed dendrite grows easily in the center of sheets due to negative TG, thus resulting in the CET [2,3]. Such non-uniform microstructure alleviates mechanical properties of the thin sheets [4,5], and how to shrink the fraction of columnar dendrite to unify the grain distribution, i.e., enhancing the CET, decides whether the thin sheets of high-performance can be obtained or not.

Enormous experimental efforts have thus been stimulated to develop various strategies to control the CET, e.g., introducing the electromagnetic field [5,6] and adding refiners [1], etc. Correspondingly, a large number of theoretical studies have also been devoted to describing accurately the mechanism of CET upon solidification. HUNT [7] first proposed that the structure of casting would grow in the form

[*] Pan WU and Jian-qi HU contributed equally in this work

Corresponding author: Feng LIU, E-mail: liufeng@nwpu.edu.cn; Shao-jie SONG, E-mail: sjsong@nwpu.edu.cn

DOI: 10.1016/S1003-6326(24)66477-0

of equiaxed grains when the volume fraction of equiaxed dendrite $f_e \geq 0.49$ holds in steady-state solidification, namely the hard blocking mechanism. Further by relaxing the assumption of constant TG, FLOOD and HUNT [8,9] introduced one-dimensional Fourier heat flow equation to deal with temperature change and proposed a specific temperature evolution equation. Considering a competitive growth between the equiaxed and the columnar grains, WANG and BECKERMANN [10,11] proposed that, if the undercooling at the columnar dendrite tip becomes sufficiently large, the equiaxed dendrite will have enough time to grow and form the equiaxed grain zone, which will hinder the growth of columnar dendrite and enhance the CET. All the above models assume the hard blocking mechanism, which, however, seems to be contradicted with many experimental results where the CET will still occur whether $f_e \geq 0.49$ holds or not. In view of this problem, MARTORANO et al [12] pointed out that the position of CET could not be judged only by the volume fraction of equiaxed dendrite, but also from the perspective of solute diffusion, namely that, only if the constitutional undercooling is exhausted, the dendritic growth stops and the CET comes into being.

Also noted that, the above theoretical works are only concerned with purely kinetic description of the dendritic growth, which, however, seems not to be consistent with actual processes including the prevailing nucleation events, especially by adding refiners. Following so-called free growth criterion proposed by GREER et al [13], the nucleation of grain is related to the refiner diameter. On this basis, how to quantitatively design the diameter of refiners to control the CET position or to enhance the CET, deserves a lot of attention.

To address the above issues, a quantitative relation between thermodynamic driving force (ΔG) and kinetic energy barrier (Q) for the dendrite growth, i.e., thermo-kinetic synergy [14−20], has been considered, including three levels, manifestation (thermo-kinetic diversity), intrinsic characteristics (thermo-kinetic correlation) and application (thermal-kinetic connection). By modifying the prevailing thermodynamics to favor the real kinetic process, the thermo-kinetic diversity is considered to explain a transition from solute diffusion to thermal diffusion [14]. Considering simultaneous dissipation by the sharp interfacial migration and diffusion, ZHANG et al [15] have constructed a physically more realistic model, which can describe quantitatively the interfacial migration (as represented by effective Q due to the mixed effect of thermal and solute diffusion) evolving against ΔG, i.e., the thermo-kinetic correlation, and thus is applied to the VTC process where sub-rapid solidification prevails. Following the thermo-kinetic connectivity [16,17], an analogous procedure for dislocation evolution upon plastic deformations was performed. Applying the thermo-kinetic correlation and connection, a new concept of generalized stability (GS) is defined as an extension and unification of the thermal and mechanical stabilities to evaluate the micro-structural evolution and/or the dynamic processes involved in both phase transformations and plastic deformations [18−20], which can be concisely expressed as

$$\Delta = \frac{Q^{\mathrm{t}}}{Q^{*}} - \frac{\Delta G^{\mathrm{t}}}{\Delta G^{*}} \tag{1}$$

with Q^{t}, Q^{*}, ΔG^{t} and ΔG^{*} having their inherent meanings at different states for different material behaviors. For example, for solidification concerned in the present work, Q^{t} and Q^{*} represent the transient and initial kinetic energy barrier for interfacial migration, respectively, while ΔG^{t} and ΔG^{*} represent the transient and initial thermodynamic driving force for interfacial migration, respectively. Following the conception of GS, many cases of metallic material design have been executed by the criterion of high ΔG−high GS, e.g., the α/γ transformation of Fe alloys has been designed to achieve outstanding strength–plasticity combination [20], and the quantitative designing of processing parameters upon VTC is realized to suppress the solidification segregation [18].

The present work aims to study the CET of Al−Mg alloys fabricated by the VTC and to quantitatively design the refiner diameters (and/or composition) by considering the thermo-kinetic synergy and the GS concept, based on a modular theoretical framework integrating the nucleation caused by refiners and the overall solidification kinetics.

2 Theoretical modeling

Upon solidification during the VTC of alloys

with refiners added, nucleation and growth need to be considered simultaneously. Here, a modular framework considering the thermo-kinetic synergy is proposed as shown in Fig. 1, where, three modules can be clearly discriminated: (1) Following the free growth criterion, the volume fraction of the inhibited nucleation zone (F_{sn}) is expressed by the undercooling (ΔT_{fg}) which introduces the nuclei number (n^*) in the nucleation stage; (2) Using the constitutional undercooling criterion, the critical nucleus radius (R_{fe}), the instantaneous nucleus radius (R_i), the liquid concentration (C_l), the concentration on liquid side at the dendrite tip (C_l^*), the liquid temperature (T_l) and the dendrite tip velocity (V) can be captured by the governing equation of growth; (3) Associating the refiner diameter (d) with ΔG and Q, the GS, the CET position (X) (i.e., the stop position of columnar growth) and the final grain size can be solved. Eventually, the material with optimized properties can be designed by the criterion of high ΔG-high GS.

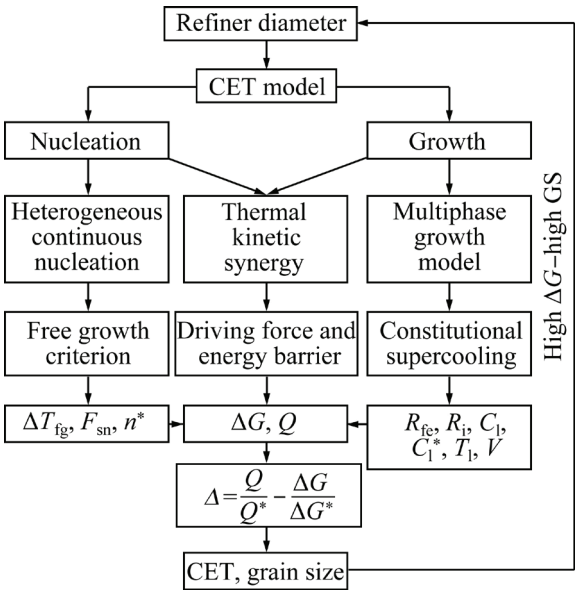

Fig. 1 Modular framework for present modeling of solidification upon VTC

2.1 Nucleation model

Under the condition of continuous nucleation with refiners added, the heterogeneous nucleation should follow the free growth criterion [13]:

$$\Delta T_{fg}=\frac{4\gamma}{\Delta S_v d}=\frac{4\Gamma}{d} \tag{2}$$

where γ is the liquid−solid interface energy, ΔS_v is the diffusion entropy per unit volume, d is the diameter of refiner, and Γ is the Gibbs−Thomson coefficient. Upon the equiaxed dendrite, the temperature will change from T_i (the melt temperature) to T_l (the liquid temperature outside the solute diffusion layer) with the distance away from nucleus as depicted in Fig. 2.

As the instantaneous equivalent dendrite envelope radius R_i increases, a inhibition nucleation zone (INZ) will form, where, with continuous advancement of solute diffusion layer, the inactivated refiners will be no longer capable of generating new grain nuclei. Once $\Delta T=\Delta T_{fg}$ holds, the thickness of INZ (i.e., the diffusion distance), δ_{INZ}, can be according to the free growth criterion expressed as

$$\delta_{INZ}=\left(\frac{\Delta T_{fg}}{\Delta T-\Delta T_{fg}}\right)R_i,\ \delta_{INZ}\in[0,\delta_d] \tag{3}$$

where δ_d is the total solute diffusion distance [21].

Suppose the refiners to be uniformly distributed within the melt, the volume fraction (F_{sn}) of these activated refiners can be expressed as [21]

$$F_{sn}=1-\frac{4\pi}{3}(R_i+\delta_{INZ})^3 n_i \tag{4}$$

where n_i is the number of refiners generated in each step of nucleation, so the number of instantaneous grains in each step can be expressed as

$$\frac{dn^*}{dt}=F_{sn}(N(d)-n^*) \tag{5}$$

where $N(d)$ is the distribution function for diameters of the refiners, as reflected by the number of refiners with diameters of [d, $d+\Delta d$] [22,23]:

$$N(d)=\frac{n_0\Delta d}{\bar{\sigma}d\sqrt{2\pi}}\exp\left[-\frac{(\ln d-\ln\bar{d})^2}{2\gamma^2}\right] \tag{6}$$

where $\bar{d}$ is the geometric mean of the diameter distribution of refiners, $\bar{\sigma}$ is the geometric standard deviation, and n_0 is the total number of nuclei during solidification. As the solidification proceeds, the solute diffusion layer expands and the nucleation process stops when the two inhibited nucleation regions impinge each other, at which $F_{sn}=0$ is satisfied.

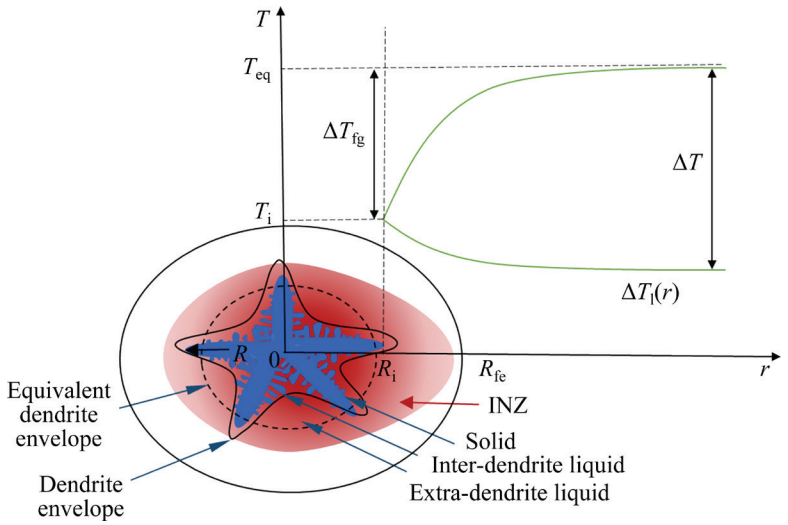

Fig. 2 Schematic diagram of local undercooling and grain envelope hypothesis with growing dendrite

2.2 Growth of CET

In the present modeling, both the dendrite envelope of columnar grain and the equiaxed grain are assumed to be spherical, where, the growth direction of columnar grains is from the casting roller wall to the center of sheet. Two key parameters, the critical nucleation radius R_{fe} and the instantaneous nucleation radius R_i must be calculated and compared. An equivalent envelope for dendritic growth with three-phase is shown schematically in Fig. 2, where, a spherical growth is assumed, so that the critical radius of grains can be solved as

$$R_{fe}=\left(\frac{3}{4\pi n^{*}}\right)^{1/3} \tag{7}$$

where n^* can be obtained by Eq. (5). Furthermore, the instantaneous nucleus radius in the growth process can be solved as

$$R_i=R_{fe}(1-f_l)^{1/3} \tag{8}$$

where f_l is the volume fraction of the extra-dendrite liquid (see Fig. 2). On this basis, the diffusion distance of grain during solidification can be solved by [23]

$$\delta_d=R_i\left(1-\frac{3}{2}R_i\frac{R_{fe}^2-R_i^2}{R_{fe}^3-R_i^3}\right) \tag{9}$$

An effective performance of the above framework requires solving the dendrite tip velocity (V), as follows [24]:

$$V=\frac{4\gamma^{*}D_l m_l(1-k)C_l^{*}}{\Gamma}(\mathrm{Iv}^{-1}(\Omega))^2 \tag{10}$$

with

$$\mathrm{Iv}^{-1}(\Omega)=0.4567\left(\frac{\Omega}{1-\Omega}\right)^{1.195} \tag{11}$$

$$\Omega=\frac{C_l^{*}-C_l}{C_l^{*}(1-k)} \tag{12}$$

where C_l^* is the concentration on liquid side at the dendrite tip, C_l is the liquid concentration, k is the non-equilibrium solute redistribution coefficient, m_l is the slope of the liquidus, and Iv^{-1} is the inverse of Ivantsov function. Thereafter, the volume fraction of liquid phase can be given as

$$S_l=\frac{3(1-f_l)^{\frac{2}{3}}}{R_{fe}} \tag{13}$$

$$-\frac{\partial f_l}{\partial t}=S_l V \tag{14}$$

where S_l is the area occupied by the equivalent envelope per unit volume upon dendritic growth (see Fig. 2). To calculate the volume fraction and the concentration change between the solid and liquid phases, the solute conservation equation for grain growth is introduced as follows:

$$(1-k)C_l^{*}\frac{\partial f_s}{\partial t}=f_{sl}\frac{\partial C_l^{*}}{\partial t}+S_l\frac{D_l}{\delta_d}(C_l^{*}-C_l) \tag{15}$$

$$\frac{\partial C_l}{\partial t}f_l=\left(S_l\frac{D_l}{\delta_d}+\frac{\partial f_l}{\partial t}\right)(C_l^{*}-C_l) \tag{16}$$

where f_s is the solid volume fraction, and f_{sl} is the volume fraction of inter-dendrite liquid, the

conservation of $f_{sl}+f_s+f_l=1$ always holds. Details to deduce Eqs. (15) and (16) are shown in Supplementary Materials (SM). Substituting Eqs. (9), (10) and (14) into Eqs. (15) and (16), the evolution of concentration and volume fraction of solid and liquid in the solidification process can be obtained.

Two inherent relations hold between the solution distribution of solid and the temperature gradient of liquid as

$$-\frac{\partial T_l}{\partial t}=\frac{H}{C_p}\frac{\partial f_s}{\partial t}-\phi \tag{17}$$

$$C_l^*=\frac{T_l-T_{eq}}{m_l} \tag{18}$$

where H is the latent heat of the alloy, C_p is the heat capacity of the alloy, ϕ is the cooling rate of the system, T_l is the liquid temperature, and T_{eq} is the equilibrium liquidus temperature. By iteration of Eqs. (17) and (18), the evolution of temperature can be obtained.

In order to deduce the CET position measured under the condition of sub-rapid solidification, the interface migration velocity by Eq. (10) and a smaller time step Δt selected (as compared to general casting solidification [21]) must guarantee the following relation [25−27]:

$$X_{t+\Delta t}=X_t+\Delta t\cdot V_{t+\Delta t} \tag{19}$$

which indicates that the growth length X of columnar crystals is related to the dendrite growth rate and the selected time step. Since the CET occurs as the growth of columnar grains stops, the CET position can be determined by iteratively solving only the length of columnar growth. The final grain radius is calculated by Eq. (7) in the final calculation step of solidification.

2.3 Thermo-kinetic synergy of CET model

Applying the present model, the CET position and the final grain radius can be predicted, provided that sufficient information for composition and processing (including refiners) is given. As mentioned in Section 1, to design the refiner for expected performance upon solidification, a thermo-kinetic modeling of ΔG, Q and GS integrating nucleation and growth is exhibited.

At the beginning of solidification, the nucleation predominates. Upon forming the nuclei, the total driving force can be expressed as [17]

$$\Delta G=\Delta G^*+f_s\Delta G_s \tag{20}$$

where f_s can be obtained according to Eqs. (13), (15) and (16), and the positive and negative driving forces, ΔG^* and ΔG_s, can be respectively derived from [28]

$$\Delta G^*=\frac{2\gamma}{R_{fe}} \tag{21}$$

$$\Delta G_s=(kC_l^*-C_l)RT_l \tag{22}$$

where γ can be obtained by the Gibbs−Thomson constant $\Gamma=\sigma/S_V$, and R is the molar gas constant. Following Ref. [28], Eq. (21) is suitable for both homogeneous and heterogeneous nucleation, from which, the increased ΔG^* corresponds to the decreased R_{fe}, which can be achieved by adding the refiner (in this work) or increasing the ΔT_{fg}.

Following Ref. [18], the effective Q can be approximated as the weighted contribution from two parts: the nucleation energy barrier Q^* and the growth energy barrier Q_s. Herein, the solid fraction, f_s, should be introduced as a weighting factor. Therefore, the total effective Q during the solidification can be obtained as

$$Q=Q^*(1-f_s)+Q_sf_s \tag{23}$$

where Q^* can be provided by the CET model as

$$Q^*=\Delta G_c=\frac{16\pi\gamma^3}{3\left(\Delta G^*\right)^2}f(\theta),\theta\in(90°,180°) \tag{24}$$

where ΔG_c is the critical nucleation work. Since the heterogeneous nucleation with refiners follows the free growth criterion, the minimum nucleation angle on the refiner should be 90° [13]. The kinetic energy barrier in the growth process Q_s can be given according to Eq. (10) as

$$Q_s=RT_l\ln\left[\frac{v_0\pi^2d(C_l-C_l^*)}{4D_l(1-k)C_l^*}\right] \tag{25}$$

where v_0 is the initial velocity of grain growth.

Following an analogous procedure by Refs. [16−20], the GS prevailing in the CET can be given as

$$\Delta=\frac{Q}{Q^*}-\frac{\Delta G}{\Delta G^*} \tag{26}$$

3 Experimental and calculation procedure

Alloy compositions of alloys in this study are listed in Table 1, where three cases including no refiners added and two alloys of refiners with different diameters added are considered. All three alloy systems have the same nominal concentration of Al−5wt.%Mg with or without refiners fabricated at the same casting speed of 2 m/min. The mean diameters of two alloys of refiners, Al−5Ti−1B and Al−5Ti−0.25C, are 0.6 and 0.8 μm, respectively [29]. Firstly, the Al ingot (99.99%) was melted in a resistance furnace heated to 750 °C. Then, the refiners of two alloys in Table 1 were added and melted until the temperature was reduced to 680 °C. The Mg bar (99.99%) was pressed into the melt through a titanium cover coated with BN coatings. After degassing and clearing off the dross, the 30%LiF−70%LiCl molten salt was first dried and then sprinkled into the melt [30].

Table 1 Parameters of Al−5wt.%Mg alloys

Alloy	Refining agent	Casting speed/ ($m \cdot min^{-1}$)
Al−5.18wt.%Mg	Without	2
Al−5.12wt.%Mg	Al−5Ti−1B	2
Al−5.15wt.%Mg	Al−5Ti−0.25C	2

The schematic illustration of twin-roll casting setup used is shown in Fig. 3. In the process of casting, the fully melted alloy is poured from the ladle into the tundish and successively flows through the core nozzle to the melt pool formed by the side dam and casting rollers. High-speed cooling water is fed into the casting rolls, and the molten alloys gradually solidify on the surface of the rolls. When passing through the roll gap, the casting rolls squeeze the solidified shells on both sides into a strip of certain thickness. The equipment parameters are listed in Table 2. In this work, the casting speed, the pressure of cooling water, and separation rolling force were 2 m/min, 0.4 MPa, and 400 kN, respectively. The as-cast and rolled sheets were obtained simultaneously by the parking methods.

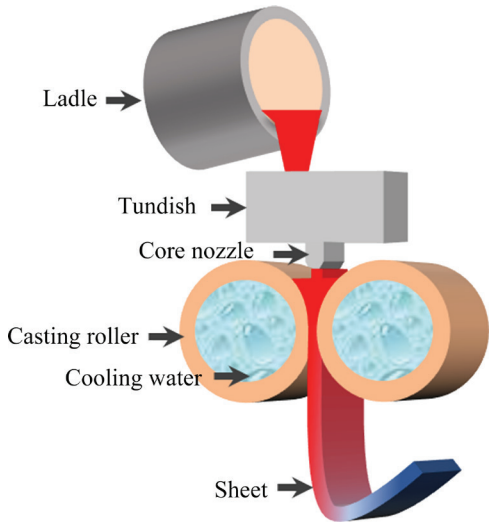

Fig. 3 Schematic diagram of twin-roll casting setup

Samples with 10 mm × 10 mm × 5 mm cubic were cut from the as-cast and rolled sheets for the three cases listed in Table 1, respectively. Position of the CET was observed with a Leica DMI5000M optical microscope (OM) after the samples were polished and etched with Keller reagent (1 mL HF + 1.5 mL HCl + 2.5 mL HNO_3 + 95 mL H_2O) for 7−8 s. Microstructure morphologies were analyzed by Helios G4 CX scanning electron microscopy (SEM). Samples for SEM investigation were etched with Keller's reagent for 3−5 min. The grain radius was determined by electron backscattered diffraction (EBSD), with step diameters of 4 and 1 μm. Samples for EBSD were electrolytically polished in a mixed solution of 10% perchloric acid and alcohol at 20 V and 0−5 °C for 10 s. The Channel-5 software was used to conduct statistical characterization of grain radius. For the micro-hardness measurement, a SHIMADZU HMV−2 microhardness tester was used with a load of 9.807 N and a holding time of 15 s. The tensile test samples were made into national standard tensile parts with thickness of 1.8 mm and total length of 90 mm. Tensile tests were carried out by an Instron

Table 2 Equipment parameters of TRC

Roller diameter/mm	Roller width/mm	Rolling force/kN	Cooling channel diameter/mm	Casting speed/($m \cdot min^{-1}$)	Pressure of cooling water/MPa
360	100	0−400	300	0−30	0−0.4

5967 universal tensile test machine equipped with video extensometer at an initial strain rate of 6.7×10^{-4} s^{-1}.

Five differential equations, i.e., Eqs. (5) and (14)−(17) are calculated to solve five variables, i.e., n^*, f_l, f_s, C_l and T_l. The initial conditions of five differential equations are applied as follows:

$$\begin{cases} n^* = 0 \\ f_l = 1 \\ f_s = 0 \\ C_l = C_0 \\ T_l = T_0 \end{cases} \tag{27}$$

The values of C_0 and T_0 are 5.0 wt.% and 937 K, respectively. Other parameters are listed in Table 3. The C_l^* and V can be directly solved by Eqs. (10) and (18) in each step, assuming to be independent on the solidification time. The fourth-order Runge-Kutta method is applied to solving these differential equations. The termination criteria of nucleation and dendrite growth respectively are

$$\begin{cases} F_{sn} = 0, \text{ nucleation stops} \\ C_l^* - C_l = 0, \text{ growth stops} \end{cases} \tag{28}$$

4 Results

4.1 Microstructures and grain radius

The microstructures of as-cast samples for the three cases in Table 1 are shown in Fig. 4, where, for all three kinds of alloys, two red lines are labeled, representing the CET position. Since the solidification of Al−Mg alloy sheet during the VTC starts from its two sides in contact with the rollers to its center, the columnar grains appear in its two sides and the equiaxed grains appear in its center (Figs. 4(a−c)). Comparing the results for cases with and without refiners, the samples without refiners have less area of equiaxed grains with a thickness of 3−3.5 mm. With the refiner of Al−5Ti−0.25C added, the area of central equiaxed grains increases and its thickness reaches 5−5.5 mm (Figs. 4(d−f)). With the refiner of Al−5Ti−1B added, the thickness of the equiaxed grain area increases to 5−6 mm (Figs. 4(g−h)). Correspondingly, the representative morphologies of grains and the histograms of grain radius distribution are exhibited in Fig. 5, where, for as-cast samples, 40% of the grains have a radius over 60 μm without refiners added (Figs. 5(a) and (d)). After adding the Al−5Ti−0.25C refiner, samples exhibit slightly refined grains ranging less

Table 3 Basic parameters used in VTC process of Al−5wt.%Mg for calculations of CET model (present model, PM)

Parameter	Value	Source
Solute diffusion coefficient, D_l/($m^2\cdot s^{-1}$)	3×10^{-9}	[27]
Melting temperature of Al, T_m/K	933.45	[27]
Gibbs–Thomson coefficient, Γ/(K·m)	2.4×10^{-7}	[27]
Partition coefficient, k	0.48	[27]
Liquidus slope, m_l/(K·wt.%$^{-1}$)	−5.84	[27]
Latent heat of melting, H/($J\cdot m^{-3}$)	9.53×10^8	[27]
Thermal conductivity of melt, α/($W\cdot m^{-1}\cdot K^{-1}$)	134	[27]
Heat capacity (298−900 K), C_p/($J\cdot m^{-3}\cdot K^{-1}$)	2.5×10^6 ($(2.43-2.92)\times10^6$)	[27]
Geometric mean of distribution, $\overline{d}$ /μm	0.77	[25]
TiB_2 refiner diameter, d_B/μm	0.6−0.8	[25]
TiC refiner diameter, d_C/μm	0.7−1.0	[29]
Geometric standard deviation, $\overline{\sigma}$	0.5	[25]
Total number of refiners (TiB_2, TiC), N/m^{-3}	2.5×10^{11}	[25]
Volume fraction of initial outer liquid phase, f_{l0}/%	99.98	PM
Volume fraction of initial solid phase, f_{s0}/%	1×10^{-2}	PM
Volume fraction of initial inner liquid phase, f_{sl0}/%	1×10^{-2}	PM
Calculation step, Δt/s	10^{-3}	PM
n_0/m^{-3}	2.5×10^{11}	PM
Alloy density, ρ/($kg\cdot m^{-3}$)	2627	[27]
Calculation tolerance, t_0	10^{-7}	PM
Initial composition, C_0/wt.%	5.0	PM
Domain diameter, d_m/mm	20	PM
Initial temperature, T_0/K	973	PM

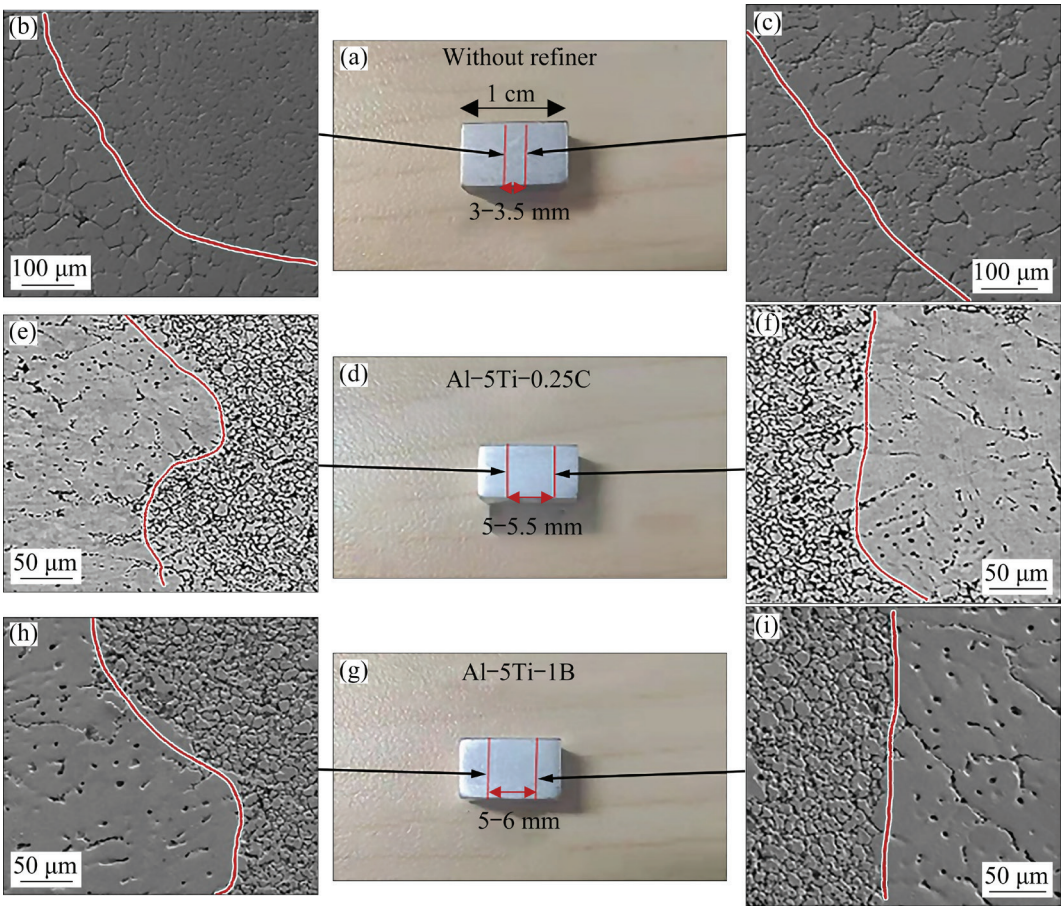

Fig. 4 Photograph and SEM observations of as-cast Al−5wt.%Mg alloys without refiners (a−c), with Al−5Ti−0.25C refiner (d−f), and with Al−5Ti−1B refiner (g−i)

than 80 μm, with an average radius of 21 μm (Figs. 5(b) and (e)), whereas, the refining of Al−5Ti−1B is more effective with the radius distribution ranging less than 70 μm and an average grain radius of 19 μm (Figs. 5(c) and (f)). Although the crystal orientation of the rolled samples seems more uniform than that of the as-cast specimen, analogous tendency with changing refiners does hold for the evolving average grain radius (Figs. 5(g−l)). This evidences the heredity of average grain radius from the as-cast to the rolled specimens.

4.2 Theoretical prediction

By the modeling in Section 2, the CET position and the grain radius can be directly solved by Eqs. (7) and (19), respectively, with the corresponding parameters listed in Table 3. Corresponding calculation results are shown for comparison with experimental results in Fig. 6. It can be seen that, for the case without refiners, the CET occurs at 3.11 mm away from the edge, in good consistency with the experimentally measured 3.5 mm. For cases with Al−5Ti−0.25C and Al−5Ti−1B refiners added, the CET positions are reduced to 2.34 and 2.21 mm, respectively, also in good consistency with the experimentally measured 2.5 and 2.3 mm (see Fig. 6(a)). The average grain radius calculated by the present model is reduced from 62 μm respectively to 17 and 14 μm by the addition of Al−5Ti−0.25C and Al−5Ti−1B, which are in good consistency with the experimentally measured evolution from 65 to 21 μm and to 19 μm, respectively (see Fig. 6(b)). Clearly, the CET can be enhanced by adding refiners, especially with Al−5Ti−1B, which expands the equiaxed dendrite area and reduces the grain radius, favoring a more uniform distribution of grain morphology.

4.3 Mechanical properties

Evolution of the hardness along the thickness of rolled sheets is presented in Fig. 7(a), where, owing to the central segregation universal in the VTC [18], the hardness in the middle corresponding

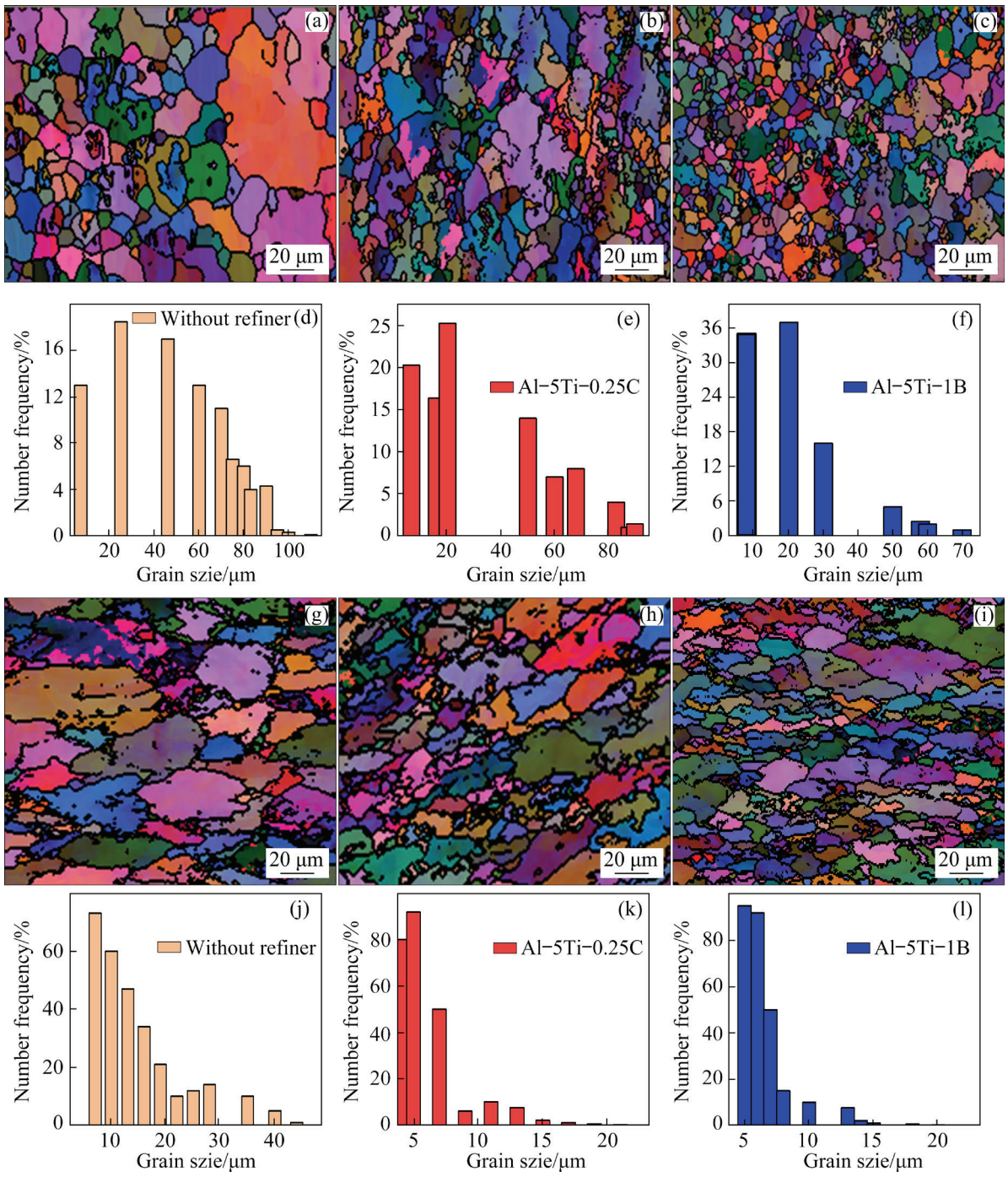

Fig. 5 EBSD images (a−c, g−i) and grain radius distribution (d−f, j−l) for as-cast (a−f) and rolled (g−l) samples without refiners (a, d, g, j), with Al−5Ti−0.25C refiner (b, e, h, k), and with Al−5Ti−1B refiner (c, f, i, l)

to the 0 mm is all lower than that on their two sides. In comparison, the higher central hardness prevails by the addition of refiners (e.g., HV 81.6 and HV 75.3 in the center), whereas, the central hardness without refiner is only HV 66.7. Further, the hardness with Al−5Ti−1B is higher than that with Al−5Ti−0.25C.

Tensile stress−strain curves of the rolled samples for three alloys are compared in Fig. 7(b), where, the yield strength (YS), the ultimate tensile strength (UTS) and the strain to failure (StF) increase simultaneously with the addition of refiner. After adding refiners, the YS and UTS of alloys with Al−5Ti−1B (145 and 217 MPa) are higher than those with Al−5Ti−0.25C (130 and 208 MPa), whereas, the StF with Al−5Ti−1B (8.2%) is lower than that with Al−5Ti−0.25C (9%).

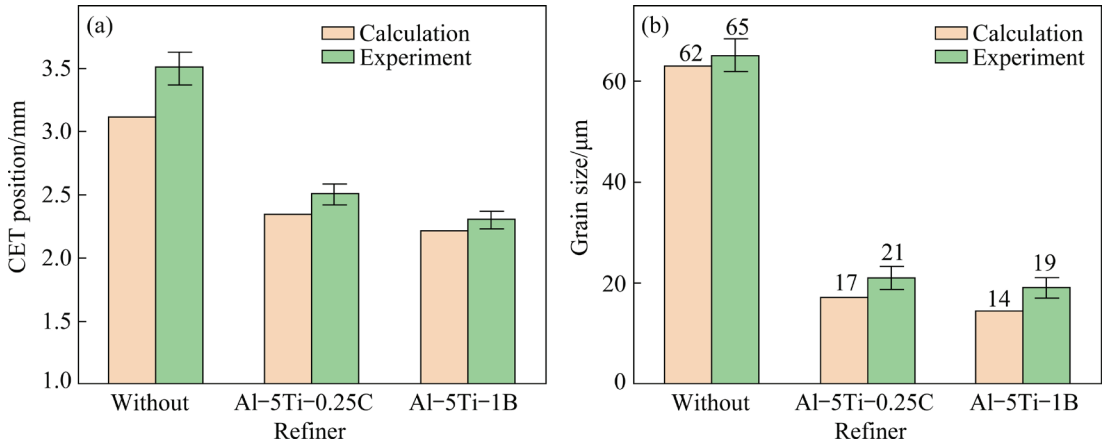

Fig. 6 Comparison of CET position (a) and grain size (b) between theoretical prediction and experimental measurement

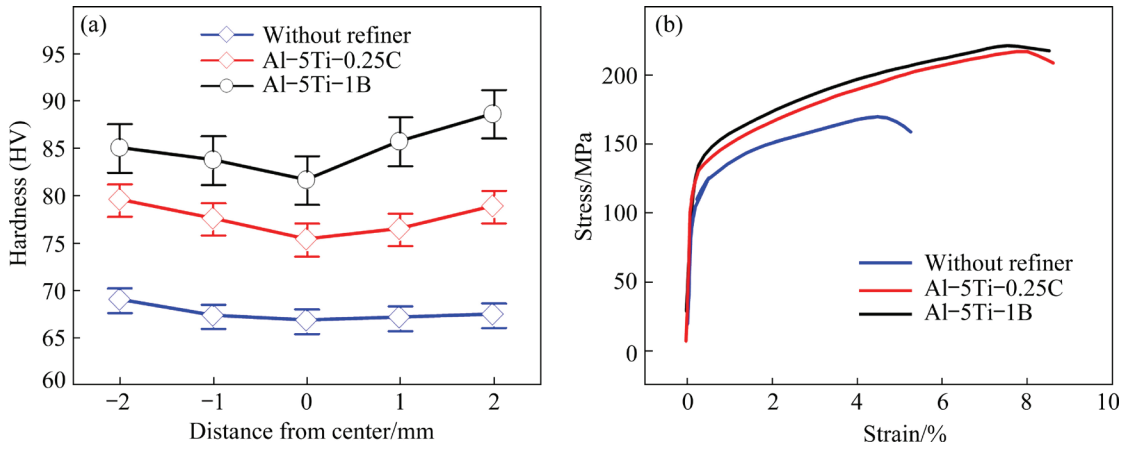

Fig. 7 Hardness (a) and stress−strain (b) curves of rolled samples for three Al−5wt.%Mg alloys

5 Discussion

In Section 4, the alloy with Al−5Ti−1B favors the larger fraction of equiaxed grains and the finer grain radius (see Fig. 6), which corresponds to the simultaneously improved strength and ductility (see Fig. 7(b)), as compared to the alloy without refiners. Firstly, the quantitative relation between the thermo-kinetic relationship for solidification (i.e., ΔG, Q, and corresponding GS) and the as-cast microstructure (i.e., CET position and grain radius) are analyzed. Secondly, the thermo-kinetic connectivity from solidification to the strength and plasticity is briefly described. Finally, based on the ΔG and GS, the refiner diameter and alloy concentration are optimized to increase simultaneously the strength and plasticity.

5.1 Thermo-kinetic analysis

Values of ΔT_{fg} for the three alloys calculated by Eq. (2) and equilibrium liquidus temperature T_{eq} calculated by commercial software Thermo-Calc are shown in Fig. 8, where, analogous to Ref. [30], different values for ΔT_{fg} show different crucial time, i.e., the beginning of nucleation, the beginning of growth, and the ending of nucleation. For the

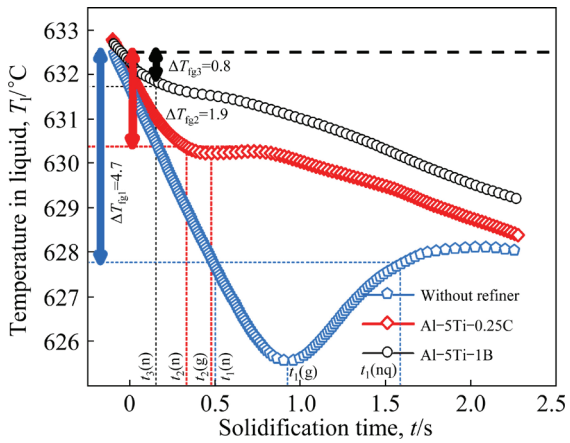

Fig. 8 Evolution of temperature T_l with solidification time t for three alloys

solidification without refiner, as for $t>t_1$(n), the condition of $\Delta T>\Delta T_{fg1}$ holds and the nucleation begins, favoring a main nucleation-controlled mechanism. As for $t>t_1$(g), the growth begins due to the recalescence corresponding to the condition of $\Delta T=\Delta T_{max}$, favoring a mainly growth-controlled mechanism. As for $t>t_1$(nq), the condition of $\Delta T>\Delta T_{fg1}$ holds and the nucleation quits, favoring a pure growth-controlled mechanism. For the solidification with the refiner of Al−5Ti−1B, the main nucleation-controlled mechanism and the main growth-controlled mechanism also hold at $t_2(n)<t<t_2$(g) and $t>t_2$(g), respectively, whereas, since a weak recalescence leads to the condition of $\Delta T>\Delta T_{fg2}$ holding for the whole post-recalescence stage, the pure growth-controlled mechanism vanishes. For the solidification with the Al−5Ti−0.25C refiner, since the absent recalescence extinguishes the t_3(g) and t_3(ng), the solidification simultaneously controlled by nucleation and growth begins as $t>t_3$(n).

By calculating Eqs. (20)−(26), values of ΔG, Q and GS can be solved, further deducing the evolution for n^* and V, as shown in Fig. 9. For the mainly nucleation-controlled stage, by adding refiners, the higher ΔG (i.e., 16.55 and 16.67 kJ/mol)) and the lower Q (calculated by Eq. (23)) for nucleation prevail, whereas, the ΔG without adding refiner is only 15.95 kJ/mol (see Fig. 9(a)) (As mentioned in Section 2.3, the higher ΔG and lower Q corresponding to the smaller R_{fg} provided by adding refiners is equivalent to increase in ΔT_{fg} [28]. Typically, by adding the refiners, the required energy fluctuation of the undercooled liquid decreases. The refiners as a heterogeneous core provide part of the driving force. Thus, the total driving force provided by adding refiners seems to be approximately equivalent to the driving force provided by the higher undercooling without refiners) (calculated by Eq. (20)). Given ΔG and Q, the GS for nucleation is calculated by Eq. (26), exhibiting the lower values (i.e., 0.121 and 0.119) with refiner (see Fig. 9(b)). After adding refiners, as the refiner diameter d decreases, i.e., from the Al−5Ti−0.25C of 0.8 μm to the Al−5Ti−1B of 0.6 μm, the increased ΔG (i.e., from 16.55 to 16.67 kJ/mol) in contrast with a decreased Q for nucleation, favors the decreased GS for nucleation (i.e., from 0.121 to 0.119). Physically, by adding smaller refiners (Al−5Ti−1B), the lower GS

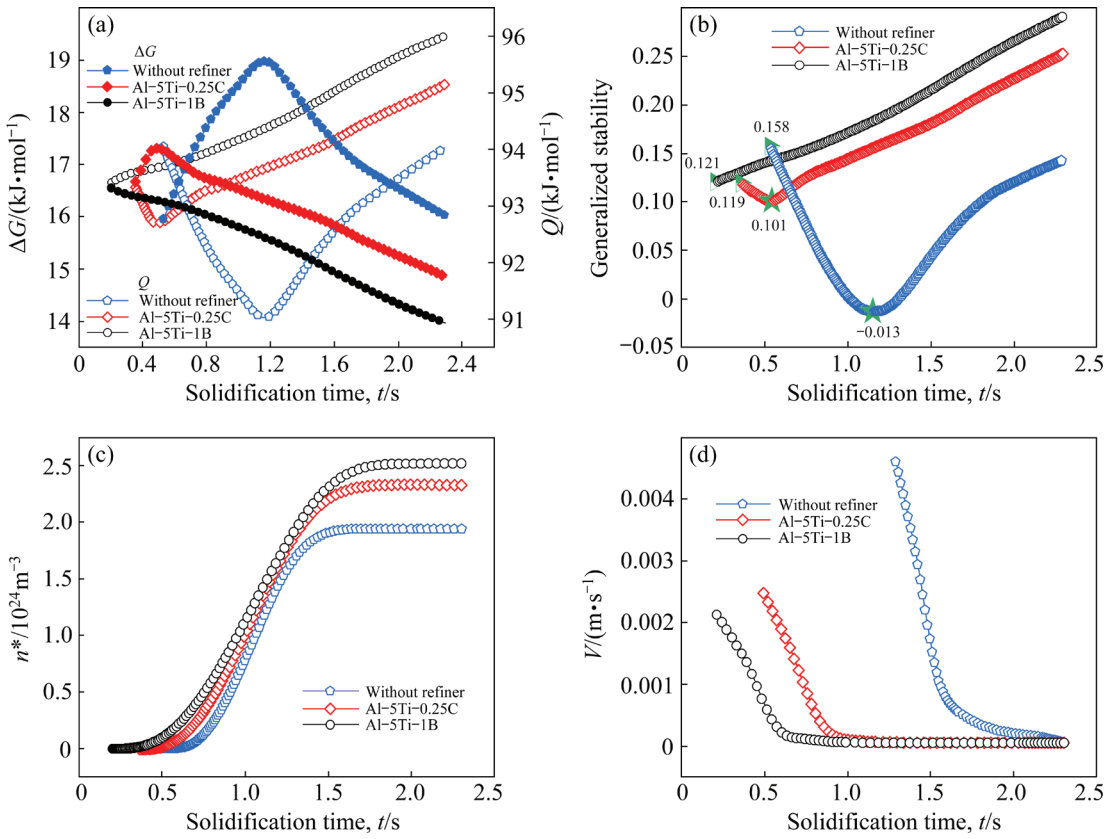

Fig. 9 Evolution of solidification parameters with time t for three alloys: (a) Thermodynamic driving force ΔG and kinetic energy barrier Q vs t; (b) Generalized stability vs t; (c) Number of nucleus n^* vs t; (d) Growth velocity V vs t

for nucleation favors a higher n^* (Fig. 9(c)), which produces a larger fraction of equiaxed grain and a lower CET position, as revealed in Fig. 6(a).

For the mainly growth-controlled stage, by adding refiners, the much lower ΔT for growth provides the much lower ΔG (16.55 and 17.31 kJ/mol) and higher GS (0.121 and 0.101), whereas, the ΔG and the GS without adding refiner are 18.97 kJ/mol and −0.013 respectively, as depicted in Figs. 9(a) and (b). After adding refiners, as the d decreases, the increased ΔG (from 16.55 to 17.31 kJ/mol) seems to be in contrast with the decreased GS for growth (from 0.121 to 0.101 kJ/mol) due to the absent recalescence. Physically, the lower GS for growth favors a higher V (Fig. 9(d)), which also produces a larger fraction of equiaxed grain and a lower CET position.

On this basis, by adding the refiner, a new strategy is thus proposed: the higher ΔG for nucleation and higher GS for growth, respectively favor the higher n^* and the lower V, producing the relatively ideal microstructure with the lower CET position and the finer grain radius. After adding the refiners, however, as d decreases, the increased ΔG for nucleation is accompanied by the decreased GS.

5.2 Design by high ΔG−high GS

As for the general cases without refiners, as ΔT_{fg} increases, the higher ΔG must be accompanied by the lower Q for the whole solidification process [18]; such trade-off relationship is called as the thermo-kinetic correlation [20]. By adding refiners, two phenomena can be summarized as follows. As compared to the case without refiners, a new thermo-kinetic trade-off balance is established, i.e., the ΔG for nucleation increases and the GS for growth decreases, particularly with the decreased refiner diameter d. As for the cases after adding refiners, the trade-off balance of high ΔG for the nucleation and low GS for the growth is broken, although the thermo-kinetic correlation also holds for both the nucleation-controlled stage and the growth-controlled stage; such event cannot be realized without refiners. As clearly shown in Fig. 9(a), the higher ΔG for nucleation is followed by the higher GS, favoring the lower CET position and finer grain radius. This philosophy seems to be closely similar to a previous article on solidification of the VTC [18], where, an artificial modulation for casting speed and speed of cooling water breaks the trade-off relationship between the initial ΔG (for nucleation) and the final GS (for growth), so that the high ΔG (suppress the centerline segregation) and the high GS (suppress the edge segregation) can be achieved simultaneously to optimize the solidification microstructure.

Following the basic procedure dealing with the criterion of high ΔG−high GS in Ref. [18], an optimized combination of parameters can be obtained to enhance the CET (Fig. 10), where, the comparison between ΔG and GS evolving with the alloy concentration C_0 and refiner diameter d is shown. As d decreases, the increased ΔG and the decreased GS (Fig. 10), respectively enhance the n^* and V, and vice versa. Analogously, as C_0 increases, the decreased ΔG and the increased GS, respectively restrain the n^* and V, and vice versa. To enhance the CET, an enhanced n^* and restrained V should be satisfied, requiring the higher ΔG and higher GS simultaneously. On this basis, a trade-off intersecting point for d and C_0 must be satisfied, before which, the higher d restrains the n^* due to the decreased ΔG and the lower C_0 improves the V due to the decreased GS, but after which, the lower d improves the V due to the decreased GS and the higher C_0 restrains the n^* due to the decreased ΔG. This philosophy can be evidenced by the present model calculations, where, following the criterion of high ΔG−high GS, an optimal combination of d=0.3 μm and C_0 of 6 wt.% Mg satisfies the relatively high n^* and low V, which enhances the CET. This result is similar to Ref. [13], where, a thorough consideration of how the modeling could direct refiner design is considered and the grain size shows a minimum as the optimal average particle diameter.

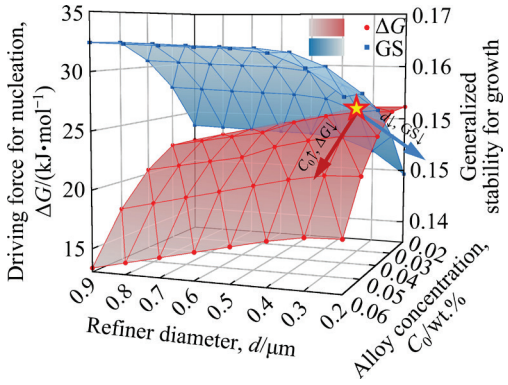

Fig. 10 Evolution of driving force for nucleation ΔG and generalized stability for growth with refiner diameter d and alloy concentration C_0

As mentioned in Section 4.3, by addition of refiners, the YS and the StF increase simultaneously, and particularly as d decreases from 0.8 μm (Al−5Ti−0.25C) to 0.6 μm (Al−5Ti−1B), the YS increases to 145 MPa but the StF decreases to 8.2%. Such favorable strength−ductility relationship should stem basically from the thermo-kinetic relationship for phase transformations [17,18,20,31,32]. According to Ref. [18], the outstanding strength–ductility resulting from the high ΔG–high GS for dislocation slip is origin from the high ΔG–higher GS for sub-rapid solidification of Al alloys. In this work, by addition of refiners, the ΔG for nucleation and the GS for growth simultaneously increase, producing the increased YS, UTS and StF. However, after adding the refiners, as for the d larger than the optimal d of 0.3 μm, although the increased ΔG and the decreased GS produced the increased YS and decreased StF (see Fig. 7(b)) simultaneously with decreased d, the slope of increased ΔG is larger than that of the decreased GS, producing the drastically increased YS and slightly decreased StF.

6 Conclusions

(1) A thermo-kinetic model for sub-rapid solidification coupling nucleation and growth is established, where, a quantitative control by a theoretical connection among refiner diameter, solidification models and as-cast microstructure has been performed.

(2) Theoretical calculation and experimental verification of CET position and grain radius with three refiners were carried out. By adding the refiners, especially Al−5Ti−1B refiner, the larger fraction of equiaxed grain and fine grain radius are exhibited, possessing simultaneously improved strength and plasticity.

(3) Through the thermo-kinetic analysis, by adding refiners, a new strategy is thus proposed, the higher ΔG for nucleation and higher GS for growth exist simultaneously, which favors the higher n^* and lower V, producing the superior microstructure with lower CET position and grain radius.

(4) Following thermo-kinetic correlation and connectivity, the superior microstructure produced by higher ΔG for nucleation and higher GS for growth, possessing the improvement of YS and StF. Based on the high ΔG–high GS criterion, the combination of 0.3 μm and Al−6wt.%Mg is optimized.

CRediT authorship contribution statement

Pan WU: Conceptualization, Methodology, Data curation, Investigation, Writing − Original draft; **Jia-qi HU:** Data curation, Investigation; **Yu-bing ZHANG:** Conceptualization, Investigation; **Shao-jie SONG:** Writing – Review & editing; **Yong LI:** Conceptualization, Data curation; **Hui-yuan WANG:** Conceptualization, Funding acquisition; **Guo YUAN:** Funding acquisition; **Feng LIU:** Conceptualization, Supervision, Funding acquisition, Resources, Writing − Review & editing.

Declaration of competing interest

The authors declare that they have no known competing financial interests or personal relationships that could have appeared to influence the work reported in this paper.

Acknowledgments

We acknowledge the financial support from the Natural Science Foundation of China (Nos. 51790481, 51790483, 52130110, 51901182), the Natural Science Foundation of Shaanxi Province, China (No. 2020JQ-157), and Research Fund of the State Key Laboratory of Solidification Processing, China (No. 2022-TS-01), and thank the Analytical & Testing Center of Northwestern Polytechnical University for equipment support.

Data availability

The processed data required to reproduce these findings cannot be shared at this time as data belong to a greater ongoing study.

Supplementary materials

Supplementary materials in this paper can be found at: http://tnmsc.csu.edu.cn/download/01-p1365-2022-1143-Supplementary_Materials.pdf.

References

[1] NG C H, BERMINGHAM M J, YUAN L, DARGUSCH M S. Towards β-fleck defect free additively manufactured titanium alloys by promoting the columnar to equiaxed transition and grain refinement [J]. Acta Materialia, 2022, 224: 117511.

[2] NGOMESSE F, REINHART G, SOLTANI H, ZIMMERMANN G, BROWNE D J, SILLEKENS W, NGUYEN-THI H. In situ investigation of the columnar-to-equiaxed transition during directional solidification of Al–

20wt.%Cu alloys on Earth and in microgravity [J]. Acta Materialia, 2021, 221: 117401.

[3] YU Wei, LI Yong, JIANG Tao, WANG Yin, ZHANG Bo-si, LI Xin-le, WANG Zhao-dong, XU Gang-ming, LI Jia-dong. Solute inverse segregation behavior in twin roll casting of an Al−Cu alloy [J]. Scripta Materialia, 2022, 213: 114592.

[4] LI Shi-ju, HE Chen, FU Jin-yu, XU Jiu-jian, XU Gang-ming, WANG Zhao-dong. Evolution of microstructure and properties of novel aluminum‑lithium alloy with different roll casting process parameters during twin-roll casting [J]. Materials Characterization, 2020, 161: 110145.

[5] CHEN Yan, ZHANG Shi-hong, SONG Hong-wu, CHENG Ming, LI Hai-hong, LIU Jin-song. Sudden transition from columnar to equiaxed grain of cast copper induced by rare earth microalloying [J]. Materials & Design, 2016, 91: 314−320.

[6] LI Shi-ju, JIANG Tao, WANG Jin-yuan, CHEN Li-zheng, WEI Bo-wen, LI Yang, XU Gang-ming, WANG Zhao-dong. Effects of different external fields on the microstructure and mechanical properties of novel Al−Cu−Li alloy during twin-roll casting [J]. Materials Science and Engineering A, 2019, 757: 14−22.

[7] HUNT J D. Steady state columnar and equiaxed growth of dendrites and eutectic [J]. Materials Science and Engineering, 1984, 65: 75−83.

[8] FLOOD S C, HUNT J D. Columnar and equiaxed growth: I. A model of a columnar front with a temperature dependent velocity [J]. Journal of Crystal Growth, 1987, 82: 543−551.

[9] FLOOD S C, HUNT J D. Columnar and equiaxed growth: II. Equiaxed growth ahead of a columnar front [J]. Journal of Crystal Growth, 1987, 82: 552−560.

[10] WANG C Y, BECKERMANN C. Prediction of columnar to equiaxed transition during diffusion-controlled dendritic alloy solidification [J]. Metallurgical and Materials Transactions A, 1994, 25: 1081−1093.

[11] WANG C Y, BECKERMANN C. Equiaxed dendritic solidification with convection: Part I. Multiscale/multiphase modeling [J]. Metallurgical and Materials Transactions A, 1996, 27: 2754−2764.

[12] MARTORANO M A, BECKERMANN C, GANDIN C A. A solutal interaction mechanism for the columnar-to-equiaxed transition in alloy solidification [J]. Metallurgical and Materials Transactions A, 2003, 34: 1657−1674.

[13] GREER A L, BUNN A M, TRONCHE A, EVANS P V, BRISTOW D J. Modelling of inoculation of metallic melts: Application to grain refinement of aluminium by Al−Ti−B [J]. Acta Materialia, 2000, 48: 2823−2835.

[14] WANG Kang, WANG Hai-feng, LIU Feng, ZHAI Hai-min. Modeling dendrite growth in undercooled concentrated multi-component alloys [J]. Acta Materialia, 2013, 61: 4254−4265.

[15] ZHANG Yu-bing, DU Jing-lian, WANG Kang, WANG Hui-yuan, LI Shu, LIU Feng. Application of non-equilibrium dendrite growth model considering thermo-kinetic correlation in twin-roll casting [J]. Journal of Materials Science & Technology, 2020, 44: 209−222.

[16] WANG Tian-le, LIU Feng. Optimizing mechanical properties of magnesium alloys by philosophy of thermo-kinetic synergy: Review and outlook [J]. Journal of Magnesium and Alloys, 2022, 10: 326−355.

[17] HE Yu-qing, SONG Shao-jie, DU Jing-lian, PENG Hao-ran, DING Zhi-gang, HOU Huai-yu, HUANG Lin-ke, LIU Yong-chang, LIU Feng. Thermo-kinetic connectivity by integrating thermo-kinetic correlation and generalized stability [J]. Journal of Materials Science & Technology, 2022, 127: 225−235.

[18] WU Pan, ZHANG Yu-bing, HU Jia-qi, SONG Shao-jie, LI Yong, WANG Hui-yuan, YUAN Guo, WANG Zhao-dong, WEI Shi-zhong, LIU Feng. Generalized stability criterion for controlling solidification segregation upon twin-roll casting [J]. Journal of Materials Science & Technology, 2023, 134: 163−177.

[19] LI Shu, ZHANG Yu-bing, WANG Kang, LIU Feng. Interface kinetics modeling of binary alloy solidification by considering correlation between thermodynamics and kinetics [J]. Transactions of Nonferrous Metals Society of China, 2021, 31: 306−316.

[20] HUANG Lin-ke, LIN Wei-tong, ZHANG Yu-bing, FENG Dan, LI Yu-jiao, CHEN Xiang, NIU Kai, LIU Feng. Generalized stability criterion for exploiting optimized mechanical properties by a general correlation between phase transformations and plastic deformations [J]. Acta Materialia, 2020, 201: 167−181.

[21] XU Yi-jiang, CASARI D, MATHIESEN R H, LI Yan-jun. Revealing the heterogeneous nucleation behavior of equiaxed grains of inoculated Al alloys during directional solidification [J]. Acta Materialia, 2018, 149: 312−325.

[22] QUESTED T E, GREER A L. The effect of the size distribution of inoculant particles on as-cast grain size in aluminium alloys [J]. Acta Materialia, 2004, 52: 3859−3868.

[23] LI Ming-jun, TAMURA T, MIWA K. Controlling microstructures of AZ31 magnesium alloys by an electromagnetic vibration technique during solidification: From experimental observation to theoretical understanding [J]. Acta Materialia, 2007, 55: 4635−4643.

[24] LIPTON J, GLICKSMAN M E, KURZ W. Dendritic growth into undercooled alloy metals [J]. Materials Science and Engineering, 1984, 65: 57−63.

[25] XU Yi-jiang, CASARI D, DU Qiang, MATHIESEN R H, ARNBERG L, LI Yan-jun. Heterogeneous nucleation and grain growth of inoculated aluminium alloys: An integrated study by in-situ X-radiography and numerical modelling [J]. Acta Materialia, 2017, 140: 224−239.

[26] MEN H, JIANG B, FAN Z. Mechanisms of grain refinement by intensive shearing of AZ91 alloy melt [J]. Acta Materialia, 2010, 58: 6526−6534.

[27] VANDYOUSSEFI M, GREER A L. Application of cellular automaton–finite element model to the grain refinement of directionally solidified Al−4.15wt.%Mg alloys [J]. Acta Materialia, 2002, 50: 1693−1705.

[28] PARK S B. Heterogeneous nucleation models to predict grain size in solidification [J]. Progress in Materials Science,

2022, 123: 100822.
[29] WANG Hai-chao, YANG Hua-bing, LIU Gui-liang, SUN Qian-qian, LIU Xiang-fa. Effect of Al−5Ti−0.25C refiner on microstructure and mechanical properties of 2024 aluminum alloy [J]. Materials Review, 2016, 20: 81−84.
[30] NING Jia-jie, LI Xiao-qian, JIANG Ri-peng, HUANG Ming-zhe. Effect of Al−5Ti−0.2C refiner on nucleation and undercooling degree of 7085 aluminum alloy [J]. Journal of Central South University (Science and Technology), 2015, 20: 19−25.
[31] ZHANG Peng, BIAN Jian-jun, ZHANG Jin-yu, LIU Gang, WEISS J, SUN Jun. Plate-like precipitate effects on plasticity of Al−Cu alloys at micrometer to sub-micrometer scales [J]. Materials & Design, 2020, 188: 108444.
[32] PENG Hao-ran, LIU Bi-shan, LIU Feng. A strategy for designing stable nanocrystalline alloys by thermo-kinetic synergy [J]. Journal of Materials Science & Technology, 2020, 43: 21−31.

双辊薄带连铸凝固过程中柱状晶向等轴晶转变的广义稳定性判据

吴 盼[1]，胡佳琦[1]，张玉兵[1]，宋韶杰[1]，李 勇[2]，王慧远[3]，袁 国[2]，刘 峰[1,4]

1. 西北工业大学 凝固技术国家重点实验室，西安 710072；
2. 东北大学 轧制与自动化国家重点实验室，沈阳 110819；
3. 吉林大学 超硬材料国家重点实验室，长春 130012；
4. 西北工业大学 分析测试中心，西安 710072

摘 要：为促进柱状晶向等轴晶转变(CET)获得均匀的等轴晶，大多数有效的理论聚焦于生长而忽略了形核的影响。为此，构建耦合细化剂异质形核和枝晶生长的理论框架，采用考虑双辊薄带连铸(VTC)凝固过程中热力学驱动力(ΔG)和动力学能垒(Q)的广义稳定性(GS)新概念，研究 CET 位置、晶粒半径和力学性能。细化剂的加入，尤其是 Al−5Ti−1B 细化剂，通过增加形核的ΔG 和生长的 GS 使晶粒半径细化到 19 μm，柱状枝晶的厚度增大到 5~6 mm，同时提高强度和塑性。遵循高ΔG −高 GS 准则，细化剂直径优化为 0.3 μm。

关键词：广义稳定性；细化剂；柱状晶向等轴晶转变；双辊薄带连铸

(Edited by Xiang-qun LI)